Bioorganic Chemistry 170 (2026) 109519

Contents lists available at ScienceDirect

Bioorganic Chemistry

journal homepage: www.elsevier.com/locate/bioorg

Sialylated porphyrins optimized as anti-infective agents against SARS-CoV-2 variants

Vivian Lioret [a], Constant Gillot [b], Marie Hologne [c], Jenny Ha [a], Dmytro Strilets [a], Laurent Lubrano Di Scampamorte [a], Laurent Gillet [c], Jonathan Douxfils [b], Stéphane P. Vincent [a,*]

[a] Research Unit of Organic Chemistry, Department of Chemistry, University of Namur, NARILIS (Namur Research Institute of Life Science), Rue de Bruxelles 61, 5000 Namur, Belgium
[b] Research Unit in Clinical Pharmacology and toxicology, Faculty of Medicine, University of Namur, NARILIS (Namur Research Institute of Life Science), Rue de Bruxelles 61, 5000 Namur, Belgium
[c] Laboratory of Immunology-Vaccinology, University of Liège, FARAH (Fundamental and Applied Research for Animals & Health), Avenue de Cureghem, 10, 4000 Liège, Belgium

ARTICLE INFO

Keywords:
Covid-19
Sialic acid
Variants of concern
Antivirals
Glycoclusters
Multivalency

ABSTRACT

Anti-adhesion strategies based on multivalent glycosylated molecules have emerged as promising antiviral tools to block early stages of viral infection. Herein, we report the design, synthesis, and evaluation of a series of porphyrin-based glycoclusters bearing sialic acid (SA) or 9-*O*-acetyl SA units, connected via linkers of varying length, polarity and rigidity. Their ability to inhibit virus-host cell interaction was assessed against wild-type, Alpha, Delta, JN.1 and KP.3 pseudotyped SARS-CoV-2 variants spanning the virus's evolutionary trajectory. The same inhibition pattern was measured with lived SARS-CoV-2 Delta variant. Although a small erosion of the SA affinity for the spike protein could be observed over the variants, all glycoclusters displayed robust and broad-spectrum neutralizing activity, highlighting the conserved role of SA-mediated recognition. Porphyrins bearing 9Ac-SA always displayed slightly better anti-effective properties than their SA counterparts. The engineering of the linkers distributing the SA ligands to the porphyrin central core proved successful as it could decrease the IC_{50}'s up to 4 times. The best optimized tetrameric inhibitors displayed a 60-fold enhanced activity compared to their monomers (15-fold per ligand). This work contributes both to the development and the improvement of antiviral agents and to a better understanding of viral evolution that drives SARS-CoV-2 infection.

1. Introduction

Late 2019 and throughout 2020, the emergence of severe acute respiratory syndrome coronavirus-2 (SARS-CoV-2) led to a global pandemic with profound health, economic and social consequences [1]. As a major threat to human health, the virus triggered an unprecedented international effort to develop both preventive (vaccines) and therapeutic strategies [2]. SARS-CoV-2, consists of a lipid envelope composed of a lipid bilayer enclosing its single-stranded RNA genome required for viral replication. The spike (S) glycoproteins are embedded in this envelop and interact with host cells by binding to angiotensin-converting enzyme 2 (ACE2) receptor, a receptor identified on epithelial cells of the respiratory tract, permitting the virus uptake [3,4]. However, for this interaction to take place, the virus must anchor to the cell surface through initial interactions with attachment factors. Several studies evidenced that heparan sulphate proteoglycans can enhance viral binding and facilitate the S protein's conformational changes [5]. Additionally, sialic acid (SA), a terminal monosaccharide found on glycoproteins and glycolipids of the host cell membrane whose interactions are well established for other coronaviruses (e.g., MERS-CoV or OC43), has a key role in mediating SARS-CoV-2 attachment as well. Indeed, several studies showed that certain domains of the S glycoprotein can bind sialylated glycans, contributing to viral tethering and tissue tropism modulation [6–18].

Given the constant mutation of the virus into new variants, the need for drug development is as topical as ever. Vaccination campaigns have been highly successful in providing global immune protection, but the appearance of immune-evasive variants has led to recurring waves of new infections [19,20]. The fight against this disease has also been waged through the prism of medicinal chemistry: drug repurposing, in

* Corresponding author.
E-mail address: stephane.vincent@unamur.be (S.P. Vincent).

https://doi.org/10.1016/j.bioorg.2026.109519
Received 3 December 2025; Received in revised form 6 January 2026; Accepted 16 January 2026
Available online 23 January 2026

particular antiviral nucleosides such as remdesivir and molnupiravir and the development of protease inhibitors [21–23].

In the quest to identify optimal strategies to counteract SARS-CoV-2, a complementary strategy has also emerged: the design of anti-adhesion molecules or materials that can be used in curative or prophylactic treatments. These agents seek to block the initial stage of infection by interfering with the virus binding to the host cells.

Glycoclusters are chemical entities of defined structures made up of multiple glycosylated motifs organised in a dense and controlled manner around a core scaffold (*i. e.* fullerene, porphyrin, …). They have emerged as powerful tools for harnessing the multivalent effect in antiviral and antibacterial strategies [24]. This effect relies on the simultaneous presentation of several sugar units capable of interacting cooperatively with viral surface proteins, typically lectins, which specifically recognise carbohydrate patterns present on host cells membranes. By amplifying these individually weak but selective interactions through multivalency, glycoclusters significantly enhance overall binding affinity to viral target, thereby blocking virus attachment and entry into host cells through an anti-adhesion mechanism. Several studies have shown that the use of multimers of D-mannose or sialic acid makes it possible to target lectins such as DC-SIGN, which are involved in infection by viruses such as HIV, Ebola and SARS-CoV [25–33].

In collaboration with the Alsteens laboratory, we previously demonstrated that 9-acetyl sialic acid (9-AcSA) exhibits higher affinity towards SARS-CoV-2 S glyco-protein compared to its non-acetylated counterpart [10]. In this study, new sialic acid glycoclusters, acetylated at C-9 position (9-AcSA) or not (SA), were designed and synthetized using fullerene, calix[4]arene, pillar[5]arene and porphyrin central cores. Their ability to inhibit the virus-host interaction was evaluated and allowed to compare the impact of both topology and valency, on the inhibition potency of these glycoclusters, including in a whole-cell infectivity assay. Among them, a porphyrin bearing four 9-AcSA displayed the most potent inhibitory effect.

In this initial discovery process we could determine that the tetravalent sialylated porphyrins **3$_a$** and **4$_a$** (Fig. 1) displayed a much higher affinity than the corresponding monomer, suggesting a multivalent binding mode to the spike protein either by chelation or quick rebinding. Moreover, interactions of sialoglycans with the N-terminal domain of the viral spike glycoprotein have been clearly identified [9] but the existence of binding phenomena between sialic acids and the spike glycoprotein at the receptor binding domain (RBD), that binds ACE2, have also been invoked [8,18]. In addition, a structural analysis of the spike glycoprotein by NMR and cryo-EM and a genetic investigation of various variant of concerns (VOCs) indicated that a distinctive sugar-binding mode mediated by the NTD of SARS-CoV-2 spike glycoprotein is lost in later variants [13].

These literature data along with our own experimental observations compel us to address the two key questions: 1) how does the affinity of sialylated porphyrins evolve as a function of the virus mutations? 2) Sialic acids having likely multiple binding pockets and binding modes with the SARS-CoV-2 S glycoprotein, can we optimize the binding efficiency of the sialylated porphyrins **3$_a$** and **4$_a$** by optimizing the way the four ligands engage contact with the S-glycoproteins?

As a rational extension of our previous study, we report herein a new generation of porphyrin-based sialic acid glycoclusters designed to address these two key questions. The objective of this work is to investigate the influence of the linker connecting the core porphyrin and the SA units towards the binding to a series of SARS-CoV-2 variants.

In previous investigations, the linker has indeed been identified to play a crucial role for optimizing the interaction with the targeted receptors [24,34,35]. Its length and rigidity may dramatically impact the avidity/multivalent effects arising from multiple binding events between the ligands and the often multimeric receptor. In the present study, we compare five pairs of glycosylated porphyrins (bearing 9-AcSA or SA) displaying lipophilic and hydrophilic linkers, of various length and conformational flexibility (Fig. 1).

The anti-infective potential of the new glycosylated porphyrins, was evaluated against five SARS-CoV-2 pseudotyped variants (wild-type D614G, Alpha B.1.1.7, Delta B.1.617.2, JN.1, and KP.3) using a standardized pseudovirus neutralization assay [36]. The inhibitory activity of each glycocluster was compared to its monomeric analogue as well as to control glycoclusters bearing non-sialylated sugars, to delineate the contribution of multivalency and to confirm the specificity of the sialic acid–spike protein interaction across different viral variants.

2. Results and discussion

2.1. Design and synthesis of the tetrasialylated porphyrins

Our original porphyrin-based glycoclusters **3$_a$** and **4$_a$** were built with

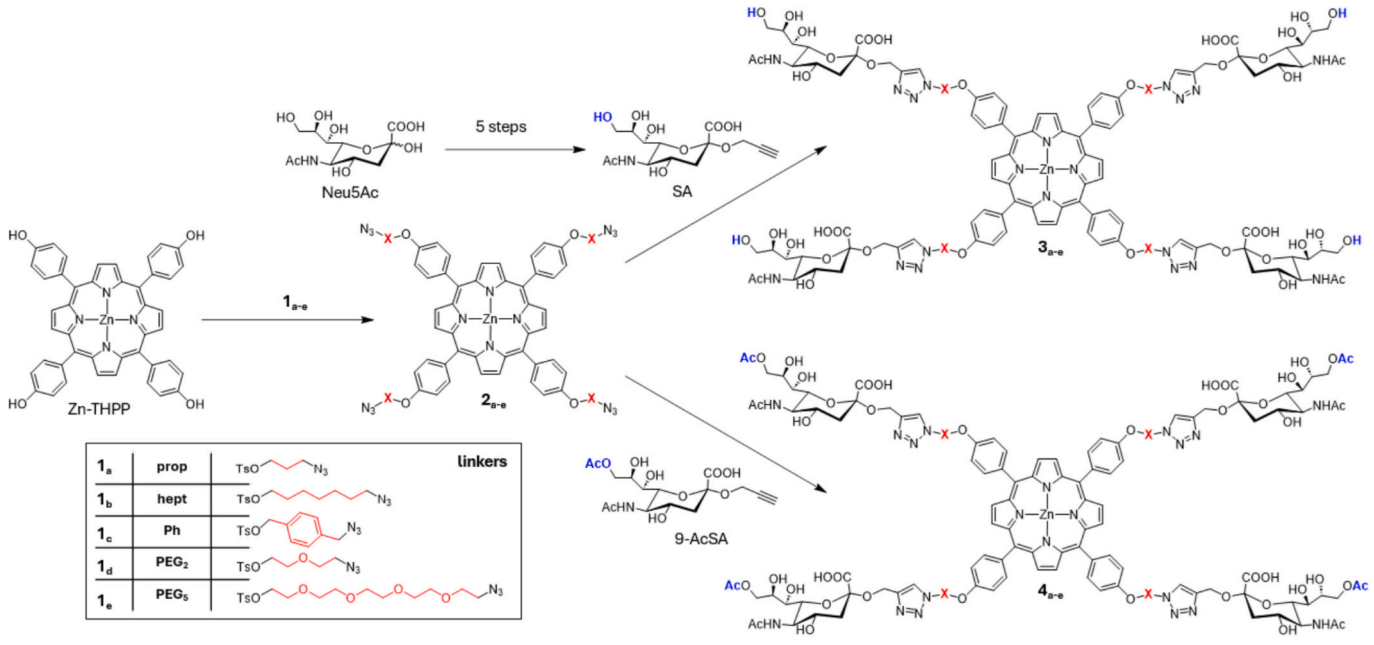

Fig. 1. Synthetic pathway to glycosylated porphyrins $3_{a\text{-}e}$ and $4_{a\text{-}e}$.

a short 3-carbon atoms linker $\mathbf{1_a}$. Lipophilicity, length and rigidity of the linker guided the selection of the novel linkers $\mathbf{1_{b\text{-}e}}$. Hydrophobic linkers $\mathbf{1_b}$ and $\mathbf{1_c}$ were selected because they are longer and $\mathbf{1_c}$ has a more limited rotational freedom. Linker $\mathbf{1_d}$ is also longer but its hydrophilic character may influence the binding processes of the 4 carbohydrate ligands. Linker $\mathbf{1_e}$ is significantly longer and hydrophilic by nature.

The general strategy to generate the porphyrins $\mathbf{3_{a\text{-}e}}$ and $\mathbf{4_{a\text{-}e}}$ consists in the grafting of the linkers to the commercially available Zn-THPP followed by a CuAAC reaction with the two clickable sialic acids SA and 9-AcSA. The synthesis of pure α-propargylated sialic acids **SA** and **9-AcSA** was realized in 5 and 6 steps, respectively, starting from commercially available *N*-acetyl-neuraminic acid following synthetic protocols already described in the literature [37,38]. The synthesis of the linker building blocks $\mathbf{1_{a\text{-}e}}$ is based on the same strategy involving an azidation followed by a tosylation of commercially available bromo-alcohols: 7-bromoheptan-1-ol, (4-(bromomethyl)phenyl)methanol, 2-(2-bromoethoxy)ethanol and 14-bromo-3,6,9,12-tetraoxatetradecanol. Thus, bromo-alcohols were first converted into the corresponding azido-alcohols via nucleophilic substitution with sodium azide in water. The resulting alcohols were then tosylated using triethylamine and DMAP, giving the desired clickable linkers in good yields (49% - 78%). Linkers $\mathbf{1_{a\text{-}e}}$ were then coupled to tetrahydroxyphenyl zinc porphyrin (Zn-THPP) through a tetra-nucleophilic substitution using potassium carbonate as a base in DMF, during 16 h at 60 °C. The resulting clickable porphyrins $\mathbf{2_{a\text{-}e}}$ were obtained in good to excellent yields (65% - 91%) as purple powders after evaporation of the solvent, addition of methanol on the solid crude and subsequent filtration and washing steps. No further purification was required.

The coupling reactions with building blocks **SA**, **9-AcSA** and tetra azidoporphyrins $\mathbf{2_{a\text{-}e}}$, was realized via microwave-assisted CuAAC in DMSO, during 4 h at 80 °C. The products were isolated by precipitation with dichloromethane followed by filtration and washing steps. Final purification by size-exclusion chromatography afforded a library of 10 tetraglycosylated porphyrins in very consistent yields (59% - 84%).

This straightforward and rational synthetic sequence allowed the access to an entire family of new sialylated porphyrins in a limited number of synthetic steps and in consistently good yields. All the intermediates were characterized by ^{1}H NMR, ^{13}C NMR and high-resolution mass spectrometry (HR-MS). Final glycoporphyrins were characterized by ^{1}H NMR, ^{13}C NMR, HRMS and HPLC-MS. The purity of the sialylated porphyrins was systematically assessed by NMR, by HRMS (SI part II) and by analytical HPLC using multiple wavelengths of detection (SI part III). In all cases, the purity was determined to be higher than 95%. In addition, a copper chelation treatment was included during the purification process to eliminate potential traces of residual copper. Finally, size exclusion chromatography ensured removal of low-molecular weight impurities, such as residual salts.

2.2. The SARS-CoV-2 neutralization potencies of final sialoporphyrins depend on the linker length and structure

The neutralizing potencies of final glycoporphyrins $\mathbf{3_{a\text{-}e}}$ and $\mathbf{4_{a\text{-}e}}$ were first evaluated against the wild type strain of SARS-CoV-2 (Fig. 2). The anti-adhesion activity of the sialoporphyrins was evaluated using a pseudovirus-based neutralization test (pVNT) employing replication-deficient Moloney murine leukemia virus (MuLV) particles pseudotyped with SARS-CoV-2 spike and a luciferase reporter gene. Viral entry into Vero-E6 cells was quantified by measuring luciferase activity 48 h post-infection and inhibitory potency was expressed as IC_{50} values (Fig. 2). All the tested compounds exhibited significant viral entry inhibitory activity with IC_{50} values between 2 mM to 33.3 μM.

A control experiment using a mannose-based glycocluster showed no inhibitory activity, confirming that selective binding processes between the sialic acid ligands and the virus is at the origin of the observed neutralizations (See SI part VIII). A similar control using monomeric forms of sialic acid **SA** and its 9-*O*-acetylated **9AcSA** showed no inhibitory activity, further confirming that the multivalent presentation of the sugar motif is essential for biological efficacy. The IC_{50} values consistently indicate that the porphyrins functionalized with 9-AcSA $\mathbf{4_{a\text{-}e}}$ display a modest yet statistically significant increase in inhibitory potency relative to their non acetylated analogues $\mathbf{3_{a\text{-}e}}$. This observation corroborates our previous findings for molecules $\mathbf{3_a}$ and $\mathbf{4_a}$ [10], reinforcing the notion that SARS-CoV-2 spike glycoprotein exhibits a higher binding affinity towards 9-*O*-acetylated sialic acid residues compared to their non-acetylated counterparts.

The initial reference porphyrins $\mathbf{3_a}$ and $\mathbf{4_a}$ displayed the lowest

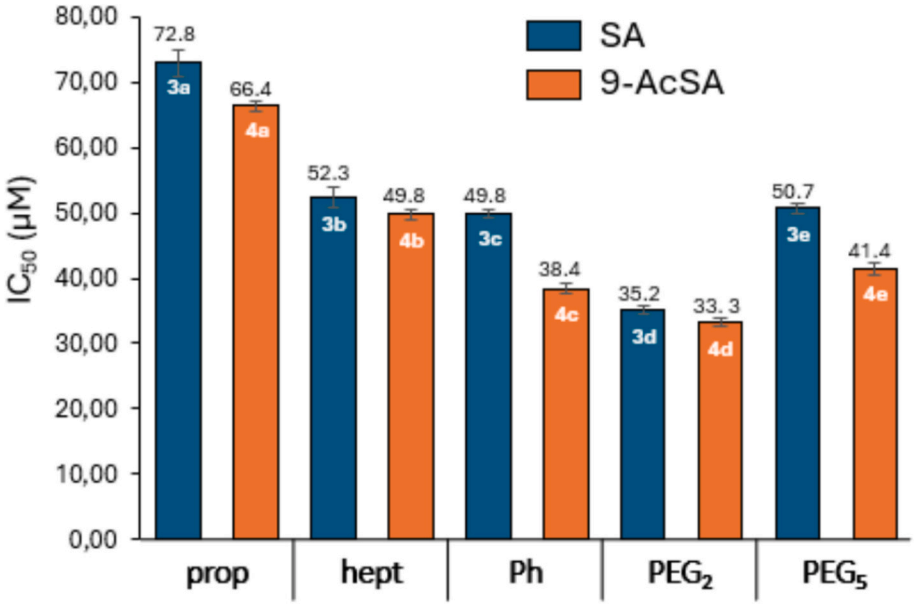

Fig. 2. Neutralizing potencies of $3_{a\text{-}e}$ and $4_{a\text{-}e}$ using replication-deficient MuLV particles pseudotyped with SARS-CoV-2 spike (wild type) and a luciferase reporter gene. Viral entry into Vero-E6 cells was quantified by measuring luciferase activity 48 h post-infection. IC_{50} values (μM) of the different glycoclusters functionalized with either SA $3_{a\text{-}e}$ (blue) or 9-AcSA $4_{a\text{-}e}$ (orange) corresponding to the number of dilutions needed of the starting solution to reach 50% of inhibition. Higher values correspond to stronger inhibitory activity. (For interpretation of the references to color in this figure legend, the reader is referred to the web version of this article.)

neutralizing potency with IC_{50} values of 72.8 μM and 66.4 μM, respectively. In our preliminary investigation, we have measured binding affinity of the tetrasialylated porphyrin **4b** towards SARS-CoV-2 spike protein by AFM [10]. The IC_{50} value obtained from this biophysical method was 5.7 μM: although not-directly comparable, this value correlates well with the IC_{50} values obtained in the present study. The aliphatic $\mathbf{3_b}$ and $\mathbf{4_b}$ and aromatic $\mathbf{3_c}$ analogues exhibited comparable inhibitory potency, with a notable exception for the compound $\mathbf{4_c}$, which presented an IC_{50} of 38.4 μM. In contrast, PEGylated porphyrins demonstrated higher inhibitory effect overall, with compound $\mathbf{4_d}$ emerging as the most potent compound in the series, with an IC_{50} of 33.3 μM.

These findings evidence two key structure-activity relationships: 1) a moderate effect of the linker length on glycocluster inhibition power, as the PEG_5 compounds $\mathbf{3_e}$ and $\mathbf{4_e}$ show a significantly lower activity than PEG_2 compounds $\mathbf{3_d}$ and $\mathbf{4_d}$ and 2) a beneficial contribution of the increased hydrophilicity introduced by PEGylated linkers, that may facilitate favourable molecular interactions.

The effect of the linker length on the final activity of the glycoclusters is clear when the best molecules **3d** and **4d** (PEG_2 linker) are compared to **3a** and **4a** bearing the shortest propyl linker. Increasing the PEG linker length (molecules **3e** and **4e**) slightly decreased the binding affinity which suggests that an optimal length was reached with molecules **3d** and **4d**. At comparable lengths, the PEG linker of **3d** and **4d** gave slightly better results than the phenyl linker of molecules **3c** and **4c** which showed that an aromatic more rigid linker does not provide an enhanced activity.

As mentioned in the introduction, the effect of valency on the biological activity of the glycoclusters. Had been already demonstrated in our initial investigation. It showed that the nature of the central core of the glycocluster impacts more the binding affinity than the valency. Porphyrins (valency 4) and fullerenes (valency 12) displayed better activities than calixarenes (valency 4) and pillararenes (valency 10) [10].

The mechanism of action of the different sialoporphyrins is expected to be identical for all studied compounds. Control experiments performed with mannose-based glycoclusters showed no inhibition, demonstrating that the observed interaction is dependent on the presence of sialic acid. Moreover, the sialic acid binding pocket of the spike has been identified in the literature, and well characterized, especially using advanced NMR techniques [9,13]. In addition, a multivalent effect is clearly observed, as reflected by the enhancement per sugar value reported in Table 1. However, it is difficult to unambiguously attribute this multivalent effect to a specific underlying mechanism (*e. g.*, chelate binding, statistical rebinding or other multivalency-related effects).

2.3. The inhibition power of the tetrasialylated porphyrins evolves as a function of SARS-CoV-2 variants

Antiviral potency of all synthesized sialoporphyrins, along with monomeric controls, were evaluated against other SARS-CoV-2 variants: Alpha, Delta, JN.1, and KP.3, selected to represent the virus's evolutionary progression over time (Table 1). Interestingly, we observed a constant erosion of the IC_{50} values over the chronological evolution of the virus. However, all compounds retained measurable inhibitory activities against all variants tested, including KP.3 lineage, known for its immune escape [39] with IC_{50} of 77.2 μM (vs 35.2 μM for the wild type) for compound $\mathbf{3_d}$ and 72.8 μM (vs 33.3 μM for the wild type) for compound $\mathbf{4_d}$. This moderate level of cross-variant effectiveness strongly contrasts with the variant-dependent loss of protection typically observed following vaccination [40].

While the overall potency decreased with viral evolution, the persistence of inhibition indicates that multivalent sialic acid-based interactions remain relevant even in the context of accumulated spike mutations.

This study also allowed us to evaluate the so-called “multivalent effect” of all glycoclusters. This effect corresponds to the enhancement of affinity of a ligand when presented as a multimer. In Table 1 are given the enhancement factors either for the tetrasialylated porphyrin vs the monomer (ratio of IC_{50}'s) or the relative multivalent effect per sugar unit (preceding factor divided by the valence 4). As the IC_{50} values for the monomers **SA** ($IC_{50} > 2$ mM) and **9-AcSA** ($IC_{50} > 2$ mM) were too high to be reliably determined under our experimental conditions, we report here only the minimal inhibition enhancement factors. Overall, a clear multivalent effect was observed for all sialoporphyrins, with compound $\mathbf{4_d}$ showing the strongest enhancement, displaying at least a 60-fold increase in binding affinity compared to its monomeric counterpart against Wild Type variant.

Consistent with previous trends, the couple of porphyrins $\mathbf{3_d}$ and $\mathbf{4_d}$ linked to SA through a PEG_2 linker were the most potent inhibitors, showing that the spike mutations did not alter the relative affinities of the final molecules. Moreover, the porphyrin bearing four 9-AcSA $\mathbf{4_d}$ slightly outperformed its analogue $\mathbf{3_d}$ across all tested variants, indicating that the beneficial effect of sialic acid acetylation at position 9 on antiviral efficacy is maintained despite the virus' spike multiple mutations.

2.4. A self-aggregation of the sialoporphyrins may contribute to multivalent effect

The present investigation evidenced a significant multivalent effect (i.e. the enhancement of the binding affinity of a receptor's ligand when displayed in a multimeric structure such as these tetrameric porphyrins).

Table 1
Inhibition data of all sialoporphyrins against different SARS-CoV-2 variants (Wild type, Alpha, Delta, JN.1, and KP.3).

	IC_{50} (μM) against SARS-CoV-2 variants					Inhibition enhancement[a], [c]	Enhancement per sugar[a], [b], [c]
	W T	Alpha	Delta	JN.1	KP.3		
SA			> 2 mM			–	–
9AcSA			> 2 mM			–	–
$\mathbf{3_a}$	72.8 ± 2.1	118.8 ± 2.3	155.4 ± 5.1	197.5 ± 8.8	261.9 ± 12.0	> 27–8	> 6.9–1.9
$\mathbf{4_a}$	66.4 ± 0.8	93.4 ± 4.3	104.4 ± 5.2	121.0 ± 4.6	159.2 ± 6.4	> 30–13	> 7.5–3.1
$\mathbf{3_b}$	52.3 ± 1.7	79.6 ± 2.3	91.8 ± 4.3	108.5 ± 3.7	143.6 ± 5.9	> 38–14	> 9.6–3.5
$\mathbf{4_b}$	49.8 ± 0.8	66.9 ± 1.1	80.4 ± 1.9	100.7 ± 2.9	140.2 ± 4.5	> 40–14	> 10.0–3.6
$\mathbf{3_c}$	49.8 ± 0.7	71.8 ± 3.3	91.3 ± 4.1	107.4 ± 2.8	134.9 ± 2.4	> 40–15	> 10.0–3.7
$\mathbf{4_c}$	38.4 ± 0.8	46.5 ± 1.6	53.6 ± 2.7	66.1 ± 2.3	74.6 ± 3.9	> 52–27	> 13.0–6.7
$\mathbf{3_d}$	***35.2 ± 0.7***	***45.8 ± 2.7***	***51.1 ± 1.9***	***58.5 ± 2.5***	***77.2 ± 3.0***	***> 57–26***	***> 14.2–6.5***
$\mathbf{4_d}$	***33.3 ± 0.7***	***40.0 ± 0.8***	***46.8 ± 1.0***	***54.8 ± 1.65***	***72.8 ± 3.6***	***> 60–27***	***> 15.0–6.9***
$\mathbf{3_e}$	50.7 ± 0.8	67.3 ± 2.3	76.7 ± 3.9	93.62 ± 2.8	123.5 ± 2.3	> 39–16	> 9.9–4.0
$\mathbf{4_e}$	41.4 ± 0.9	56.1 ± 0.9	63.4 ± 3.0	75.5 ± 2.5	106.2 ± 4.3	> 48–19	> 12.1–4.7

[a] Range is given from highest value (obtained against WT variant) to lowest value (obtained with KP.3).
[b] Enhancement per sugar = IC_{50}monomer/(IC_{50}porphyrin/4).
[c] Actual enhancement values are higher than those displayed for clarity, since IC_{50}monomers > 2 mM (value could not be measured above 2 mM).

A multivalent effect may either be due to a quick rebinding process of the sialic acids to the spike protein or to an increased local concentration effect. If the latter mechanism operates, aggregates of the glycoclusters may account for the multivalent effect. Porphyrins in general have the propensity to stack and aggregate in aqueous solution, through well-defined π-stacking processes [41,42]. It is thus possible that the anti-infective activities of the sialoporphyrins arise from or are amplified by their aggregation.

To assess the aggregation properties of the final molecules $\mathbf{3_{a\text{-}e}}$ and $\mathbf{4_{a\text{-}e}}$, Dynamic Light Scattering (DLS) measurements were performed at concentration ranging from 250 μM to 16 μM. These analyses revealed the presence of two main size populations: hydrodynamic diameter in the range of 1–5 nm corresponding to the monomeric form of the molecules and the size population between 100 and 300 nm attributed to aggregated assemblies observed across all tested concentrations (SI part IV). In general, the polydispersity indexes of the solutions increased upon dilution, indicating instability or dissociation of aggregates. For instance, we also measured DLS at a concentration of 8 μM for all compounds, but the polydispersity indexes were systematically too high to provide interpretable data (data not shown). Overall, these results are in accordance with weakly cooperative aggregation behaviour in aqueous solution.

Furthermore, aggregated particles were observed using advanced microscopy techniques, such as Transmission Electron Microscopy (TEM) and Atomic Force Microscopy (AFM). TEM and AFM images of $\mathbf{3_a}$ showed aggregated nanoparticles (100–300 nm) that are composed of small spherical subunits up to 10 nm in size (presumably non-aggregated compounds). Moreover, AFM confirms the presence of 2 size populations: small spherical nanoparticles with size up to 8 nm and aggregated assemblies with sizes up to 200 nm (SI part V & VI).

Compounds $\mathbf{3_{a,d}}$ and $\mathbf{4_{a,d}}$ were also analysed by UV–Visible absorbance spectroscopy: the analyses were recorded in water at lower concentrations (from 20 μM to 0.63 μM). As shown in part VII (SI), no spectral features typically associated with porphyrin π-stacking aggregation (i.e., broadening or red shifting of the Soret band) were observed. Instead, a linear correlation was observed between the maximum absorbance and the concentration (up to 5 μM), indicating that the porphyrins are unlikely to self-assemble as π-stacking aggregates. The aggregates detected by DLS at low concentrations may thus originate from interactions distinct from π-stacking, for instance from electrostatic or hydrophilic interactions mediated by the sugar substituents.

Overall, these data show that all porphyrins do have comparable aggregation properties, regardless of the structure and nature of the linkers to which are attached the four ligands. This aggregation may contribute to the observed multivalent effect by increasing the local concentration of ligands and/or favor the statistical ligand rebinding to the spike protein.

2.5. Optimized compounds 3_d and 4_d display antiviral activity against lived Delta variant

To further evaluate the inhibitory activity of the most potent sialoporphyrins, antiviral efficacy was assessed using a Focispot reduction assay in Vero ACE2 cells. Compounds $\mathbf{3_d}$ and $\mathbf{4_d}$ were tested across a range of concentrations against lived Delta variant virus. Viral replication was detected by immunostaining with a biotinylated monoclonal antibody and HRP-conjugated streptavidin. The number of infectious foci was quantified using an automated reader, and inhibition was expressed relative to untreated virus controls (Fig. 3). Both compounds exhibited a comparable, dose-dependent reduction in infectious foci formation, demonstrating similar antiviral activity across the concentrations range (0.01 μM - 100 μM). The IC_{50} values were 7.19 μM and 8.37 μM respectively for $\mathbf{3_d}$ and $\mathbf{4_d}$. These results are particularly encouraging, as the assay mimics near physiological conditions using live virus on host cells, providing a relevant measure of antiviral efficacy in a biologically meaningful context.

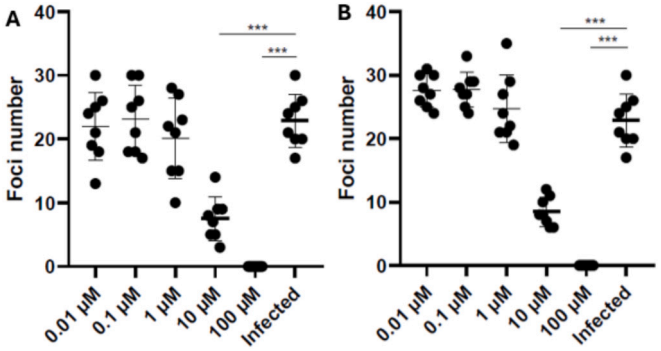

Fig. 3. Dose-dependent inhibition of SARS-CoV-2 lived Delta variant by compounds 3_d (A) and 4_d (B) in Vero ACE2 cells measured by Focispot assay.

2.6. Cytotoxicity evaluation

The cytotoxicity of the molecules was evaluated using a crystal violet staining test. Vero-E6 cells were deposited in wells and the molecules were tested at 2 mM, 200 μM and 20 μM and deposited on the cells. Twenty-four hours later, the supernatant was discarded, and the cells were fixed with 4% paraformaldehyde for 30 min. The living cells were then stained with a 1% crystal violet solution for 30 min. This stain was then resuspended with methanol and the absorbance of the different wells was read at 580 nm using the SpectraMax iD3. Among all the molecules tested at the concentrations tested, none demonstrated the ability to induce at least 50% cytotoxicity, so the EC_{50} values of the molecules are above 2 mM.

3. Conclusion

In summary, a series of novel porphyrin-based sialic acid glycoclusters, displaying five different types of linkage between the SA or 9-AcSA units and the porphyrin core were efficiently prepared using a final microwave-assisted click chemistry approach. The characterizations and the assessment of the purity of all final molecules were realized using NMR, HRMS and HPLC analyses. The entire family of new glycoporphyrins displayed good inhibitory activity against five variants of SARS-CoV-2 delineating the evolutionary trajectory of the virus. Among them, the most potent compound has been found to be PEG_2-linked glycocluster bearing 9-AcSA, maintaining excellent efficiency across pseudotyped variants, but also displaying strong inhibition properties against lived Delta variant ($IC_{50} < 10$ μM). Our data evidenced a continuous and moderate erosion of the binding avidity of the SARS-CoV-2 virus variants towards sialylated conjugates. This diminution was predicted by Buchanan et al. based on the fact that SARS-CoV-2 variants possess hotspot mutations in the NTD of the spike protein, thus hampering SA binding [13]. However, the present studies shows that the loss of binding activity of our initial sialoporphyrins $\mathbf{3_a}$ and $\mathbf{4_a}$ from wild type SARS-CoV-2 to KP.3 could be compensated by engineering the linkers connecting the four SA and the central porphyrin. This implies that SARS-CoV-2 retains a strong ability to exchange sialic acid-mediated interactions for host cell engagement. These results are in deep contrast with the variant-dependent loss of protection typically observed following vaccination.

Our results highlight the effectiveness of the multivalent approach in targeting SARS-CoV-2 viral adhesion mechanisms, as all final molecules displayed enhanced inhibitory activities. For the best molecule the affinity of each sialic acid unit of the porphyrin tetramer is enhanced by a factor of at least 15 compared to monomeric SA. An analysis by DLS, electron microscopy and AFM showed that the natural self-aggregation properties of porphyrins may contribute to the enhancement of affinity of SA when displayed as a tetramer around a porphyrin scaffold. The fact that a PEG linker with an optimal length gave the best results suggests

that the conformational and rotational freedom left by the PEG_2 linker favours the association of SA and the spike protein. Altogether, a mechanism involving either a quick rebinding of the SA ligands to the spike or a chelation process likely explains the observed multivalent effect.

The compounds developed in this study were not designed as small-molecule antiviral drugs as they do not meet conventional drug-likeness criteria due to their large molecular weight and volume. Rather, their foreseen application is their use as multivalent decoy antiadhesive molecules to interfere with sialic acid-dependent interactions, in order to prevent the viral accumulation at the lung epithelium. In this context, potential local administration routes, such as intranasal delivery with nasal spray formulation, would represent a more relevant and realistic mode of use.

In addition, this study confirms the moderate preference of the spike glycoprotein to bind to 9-AcSA over SA whatever the degree of mutation of the spike glycoprotein. Importantly, the linker screening, varying length, rotational freedom, and lipophilicity, allowed the identification of multivalent structures with improved activity: the optimized compound **4_d** display meaningful yet moderate IC_{50} values against the "most recent" variant (72.8 μM), whereas the non-optimized molecule **3_a** shows much weaker activity (IC_{50} = 261.9 μM). This demonstrates that, although the overall effect of these linker properties is modest within the tested chemical space, its systematic variation can lead to functionally meaningful improvements in multivalent inhibitor potency. This work contributes both to the development and the improvement of antiviral agents and to a better understanding of viral evolution that drives SARS-CoV-2 infection. In particular, our results suggest that sialylated porphyrins retain similar binding activity across the tested variants, indicating a lower sensitivity to the mutations of the spike protein examined here. While this in vitro observation cannot be extrapolated to in vivo efficacy, nor replace or compete with vaccination, it contrasts the well-documented mutation-dependence of vaccine effectiveness, where specific viral mutation can reduce immune recognition. This highlights the potential of this approach as a mutation-tolerant molecular recognition strategy.

4. Experimental section

4.1. Chemistry

All reactions were carried out under argon atmosphere and dried glassware. Solvents were purchased in industrial grade and further distilled before their use. Reagents and chemicals were purchased from Merck, Acros and PorphyChem at ACS grade and were used without purification. All reactions were monitored by thin-layer chromatography (TLC) carried out on Merck aluminium roll silica gel 60-F_{254} using $KMnO_4$ as revelators. Merck silica gel (60, particle size 40–63 μm) was employed fir column chromatography. NMR spectra were recorded on a JEOL KMN EX-500 with solvent peaks as reference. The chemical shifts were reported in parts per million (ppm), the coupling constant (J) were expressed in hertz (Hz) and signals were described as singlet (s), doublet (d), triplet (t) as well as multiplet (m). HR-ESI-MS data were acquired on Brucker MaXis mass spectrometer Q-TOF. RP-HPLC-MS analyses were performed on a Aliance Waters 1642 instrument equipped with a diode array detector (UV–Vis 2489 Waters detector) and Acquity Waters QDa detector mass spectrometer. See Supporting Information for all details related to instruments and methods for characterizations of synthetized compounds and for spectrum. Compounds SA, 9-AcSA, **3_a** and **4_a** were synthesized following published methods [10].

4.1.1. General procedure for linker $1_{a\text{-}e}$ synthesis

To a solution of Bromo alcohol (1 equiv.) in water (1 g/10 mL) was added sodium azide (2.2 equiv.). the reaction mixture was stirred overnight at 60 °C. the solution was then extracted with DCM and the organic phase was dried over $MgSO_4$ and concentrated under reduced pressure. The isolated oil was directly diluted in DCM (1 g/15 mL) and DMAP (0.1 equiv.), tosyl chloride (1.2 equiv.) and triethylamine (1.4 equiv.) were added to the solution. The reaction mixture was stirred during 4 h at room temperature. The solution was concentrated under reduced pressure and the crude was purified over silica gel column chromatography.

Linker **1_a**: 3-bromo-propan-1-ol (5.00 g) was used as starting material. Crude was purified over silica gel column chromatography (Cyclohexane/EtOAc 95:5 to 8:2) to obtain compound **1_a** as crystalline solid (6.41 g, 70%). Characterisations were in accordance with the literature [43].

Linker **1_b**: 7-bromo-1-heptanol (1.00 g) was used as starting material. Crude was purified over silica gel column chromatography (Cyclohexane/EtOAc 9:1 to 8:2) to obtain compound **1_b** a colourless oil (1.16 g, 73%). ^{1}H NMR (500 MHz, $CDCl_3$) δ 7.79 (d, J = 8.2 Hz, 2H), 7.35 (d, J = 8.2 Hz, 2H), 4.02 (t, J = 6.4 Hz, 2H), 3.24 (t, J = 6.9 Hz, 2H), 2.45 (s, 3H), 1.64 (dq, J = 13.0, 6.5 Hz, 2H), 1.59–1.51 (m, 2H), 1.36–1.26 (m, 6H). ^{13}C NMR (126 MHz, $CDCl_3$) δ 144.84, 133.28, 129.96, 128.03, 70.63, 51.48, 28.84, 28.81, 28.59, 26.61, 25.36, 21.79.

Linker **1_c**: 4-(Bromomethyl)benzenemethanol (500 mg) was used as starting material and the first step was done in DMF. Crude was purified over silica gel column chromatography (Cyclohexane/EtOAc 95:5) to obtain compound **1_c** a colourless oil (219 mg, 49%). The tosylated compound was not obtained, but the chlorinated version instead. ^{1}H NMR (500 MHz, $CDCl_3$) δ 7.39 (d, J = 6.5 Hz, 2H), 7.32 (d, J = 7.9 Hz, 2H), 4.60 (s, 2H), 4.33 (s, 2H). ^{13}C NMR (126 MHz, $CDCl_3$) δ 137.73, 135.80, 129.22, 128.68, 54.51, 45.88.

Linker **1_d**: 2-(2-bromoethoxy)ethanol (1.00 g) was used as starting material. Crude was purified over silica gel column chromatography (Cyclohexane/EtOAc 4:6) to obtain compound **1_d** a colourless oil (1.44 g, 78%). ^{1}H NMR (500 MHz, $CDCl_3$) δ 7.81 (d, J = 8.3 Hz, 2H), 7.35 (d, J = 8.5 Hz, 2H), 4.17 (dd, J = 5.3, 4.1 Hz, 2H), 3.70 (dd, J = 5.3, 4.1 Hz, 2H), 3.61 (dd, J = 5.5, 4.5 Hz, 2H), 3.30–3.33 (m, 2H), 2.45 (s, 3H). ^{13}C NMR (126 MHz, $CDCl_3$) δ 145.60, 133.49, 130.53, 128.67, 70.87, 69.79, 69.36, 51.29, 22.34.

Linker **1_e**: 14-bromo-3,6,9,12-tetraoxatetradecan-1-ol (500 mg) was used as starting material and the first step was done in DMF. Crude was purified over silica gel column chromatography (DCM/MeOH 98:2) to obtain compound **1_e** a colourless oil (358 mg, 53%).^{1}H NMR (500 MHz, $CDCl_3$) δ 7.80 (d, J = 8.3 Hz, 2H), 7.34 (d, J = 8.5 Hz, 2H), 4.16 (dd, J = 5.4, 4.3 Hz, 2H), 3.70–3.67 (m, 4H), 3.66 (s, 4H), 3.65–3.60 (m, 4H), 3.59 (s, 4H), 3.40–3.37 (m, 2H), 2.45 (s, 3H)·^{13}C NMR (126 MHz, $CDCl_3$) δ 144.95, 133.10, 129.97, 128.14, 70.90, 70.84, 70.80, 70.77, 70.66, 70.18, 69.39, 68.82, 50.81, 21.80.

4.1.2. General procedure for porphyrin platforms $2_{a\text{-}e}$ synthesis

To a solution of zinc (II) 5,10,15,20-(tetra-4-hydroxyphenyl) porphyrin Zn-THPP (1 equiv.) and potassium carbonate (6 equiv.) in DMF (100 mg/5 mL) was added compounds **1a-e** (6 equiv.). the reaction mixture was stirred overnight at 70 °C. the solution was concentrated under reduced pressure and MeOH was added to the crude. The suspension was filtered and washed with MeOH and water.

*Porphyrin **2a***: Starting Zn-THPP (200 mg) react with **1a** (413 mg) and potassium carbonate (223 mg) to yield compound **2a** as a purple solid (249 mg, 86%). Characterizations are in accordance with the literature [43].

*Porphyrin **2b***: Starting Zn-THPP (100 mg) react with **1b** (252 mg) and potassium carbonate (112 mg) to yield compound **2b** as a purple solid (150 mg, 85%). ^{1}H NMR (500 MHz, $CDCl_3$) δ 8.98 (s, 8H), 8.11 (d, J = 8.4 Hz, 8H), 7.27 (d, J = 8.7 Hz, 8H), 4.25 (t, J = 6.4 Hz, 8H), 3.26 (t, J = 6.9 Hz, 8H), 2.01–1.96 (m, 8H), 1.65 (m, 16H), 1.52–1.47 (m, 16H). ^{13}C NMR (126 MHz, $CDCl_3$) δ 158.85, 150.62, 135.56, 135.32, 131.99, 120.87, 112.66, 68.28, 51.46, 29.55, 29.16, 28.86, 26.81, 26.27.

*Porphyrin **2c***: Starting Zn-THPP (112 mg) react with **1c** (164 mg) and potassium carbonate (125 mg) to yield compound **2c** as a purple solid (180 mg, 90%). ^{1}H NMR (500 MHz, DMSO-d_6) δ 8.80 (s, 8H), 8.08 (d, J

= 7.9 Hz, 8H), 7.69 (d, J = 7.6 Hz, 8H), 7.52 (d, J = 7.5 Hz, 8H), 7.43 (d, J = 8.0 Hz, 8H), 5.40 (s, 8H), 4.54 (s, 8H). ^{13}C NMR (126 MHz, DMSO-d_6) δ 157.93, 149.58, 137.19, 135.40, 135.23, 131.57, 128.74, 128.45, 119.94, 112,89, 99.50, 69.29, 53.41. HRMS (ESI+) calculated for $C_{76}H_{57}N_{16}O_4Zn$ $[M + H]^+$: 1321.4035, found: 1321.3991.

*Porphyrin **2d***: Starting Zn-THPP (105 mg) react with **1d** (242 mg) and potassium carbonate (117 mg) to yield compound **2d** as a purple solid (152 mg, 91%). ^{1}H NMR (500 MHz, $CDCl_3$) δ 8.96 (s, 8H), 8.12 (d, J = 8.2 Hz, 8H), 7.29 (d, J = 8.5 Hz, 8H), 4.44–4.40 (m, 8H), 4.04–4.01 (m, 8H), 3.85–3.81 (m, 8H), 3.47–3.43 (m, 8H). ^{13}C NMR (126 MHz, $CDCl_3$): δ 158.45, 150.60, 135.76, 135.55, 132.03, 120.77, 112.84, 70.35, 70.04, 67.78, 50.73. HRMS (ESI+) calculated for $C_{60}H_{57}N_{16}O_8Zn$ $[M + H]^+$: 1193.3831, found: 1193.3806.

*Porphyrin **2e***: Starting Zn-THPP (106 mg) react with **1e** (358 mg) and potassium carbonate (118 mg) to yield compound **2e** as a purple solid (160 mg, 65%). ^{1}H NMR (500 MHz, $CDCl_3$) δ 8.95 (s, 8H), 8.10 (d, J = 8.3 Hz, 8H), 7.29 (d, J = 8.4 Hz, 8H), 4.44–4.42 (m, 8H), 4.05–4.03 (m, 8H), 3.86–3.84 (m, 8H), 3.78–3.75 (m, 8H), 3.70 (m, 16H), 3.67–3.61 (m, 8H), 3.62–3.58 (m, 8H), 3.50 (t, J = 5.0 Hz, 8H), 3.15 (t, J = 5.0 Hz, 8H). ^{13}C NMR (126 MHz, $CDCl_3$) δ 158.52, 150.53, 135.70, 135.53, 131.97, 120.69, 112.85, 71.00, 70.76, 70.75, 70.71, 70.66, 70.05, 69.96, 67.80, 50.51. HRMS (ESI+) calculated for $C_{84}H_{105}N_{16}O_{20}Zn$ $[M + H]^+$: 1721.6977, found: 1721.6977; calculated for $C_{84}H_{106}N_{16}O_{20}Zn$ $[M + 2H]^{2+}$: 861.3525, found: 861.3515.

4.1.3. General procedure for glycoclusters $3_{a\text{-}e}$ synthesis

To a solution of porphyrins $\mathbf{2_{a\text{-}e}}$ (1 equiv.) and CuBr.DMS (0.6 equiv.) in DMSO (30 mg/mL) was added sialic acid **SA** (5 equiv.). The reaction mixture was stirred under microwave irradiation at 80 °C for 4 h. The product was precipitated by addition of DCM and the recovered solid was dissolved in water and treated with QuadrasilMP. The product was purified over size exclusion chromatography on Sephadex G-25 (eluant: water).

Glycocluster $\mathbf{3_a}$: Porphyrin $\mathbf{2_a}$ (31.0 mg) was reacted with **SA** (50.0 mg) and CuBr.DMS (3.5 mg) to yield compound $\mathbf{3_a}$ as a purple solid after lyophilisation (59.0 mg, 84%). Characterisations are in accordance with the literature [10].

Glycocluster $\mathbf{3_b}$: Porphyrin $\mathbf{2_b}$ (22.4 mg) react with **SA** (30.0 mg) and CuBr.DMS (2.1 mg) to yield compound $\mathbf{3_b}$ as a purple solid after lyophilisation (39.0 mg, 84%). ^{1}H NMR (500 MHz, MeOD-d_4) δ 8.83 (s, 8H), 8.08–7.96 (m, 12H), 7.21 (s, 8H), 4.97 (d, J = 11.5, 4H), 4.69 (d, J = 11.4, 4H), 4.41 (t, J = 6.4, 8H), 4.21–4.11 (m, 8H), 3.92–3.81 (m, 8H), 3.77–3.72 (m, 8H), 3.67–3.61 (m, 8H), 3.55–3.50 (m, 4H), 2.84 (d, J = 10.9, 4H), 2.00 (s, 12H), 1.98–1.94 (m, 8H), 1.92–1.86 (m, 8H), 1.73–1.64 (m, 4H), 1.63–1.55 (m, 8H), 1.54–1.47 (m, 8H), 1.44–1.36 (m, 8H). ^{13}C NMR (126 MHz, DMSO-d_6) δ 172.67, 158.29, 149.70, 144.70, 135.28, 134.95, 131.60, 123.84, 120.10, 112.64, 99.55, 73.04, 71.54, 69.22, 67.73, 67.17, 63.42, 57.39, 53.28, 49.39, 29.81, 28.97, 28.38, 26.02, 25.63, 22.60. HRMS (ESI+) calculated for $C_{128}H_{166}N_{20}O_{40}Zn$ $[M + 2H]^{2+}$: 1343.5425, found: 1343.5435; calculated for $C_{128}H_{167}N_{20}O_{40}Zn$ $[M + 3H]^{3+}$: 896.0308, found: 896.0308; calculated for $C_{128}H_{168}N_{20}O_{40}Zn$ $[M + 4H]^{4+}$: 672.2749, found: 672.2756. HPLC analysis 2.68 min, 75.4% MeCN.

Glycocluster $\mathbf{3_c}$: Porphyrin $\mathbf{2_c}$ (22.8 mg) react with **SA** (30.0 mg) and CuBr.DMS (2.1 mg) to yield compound $\mathbf{3_c}$ as a purple solid after lyophilisation (38.7 mg, 83%). ^{1}H NMR (500 MHz, MeOD-d_4) δ 8.85 (s, 8H), 8.10 (d, J = 8.3, 8H), 8.04 (s, 4H), 7.68 (d, J = 8.1, 8H), 7.47 (d, J = 8.1, 8H), 7.39 (d, J = 8.4, 8H), 5.67 (s, 8H), 5.38 (s, 8H), 4.97 (d, J = 12.3, 4H), 4.70 (d, J = 12.2, 4H), 3.90–3.81 (m, 8H), 3.72 (dd, J = 7.1, 1.9, 8H), 3.65–3.60 (m, 8H), 3.52 (dd, J = 9.1, 1.7, 4H), 2.89–2.83 (m, 4H), 2.00 (s, 12H), 1.62 (t, J = 11.9, 4H). ^{13}C NMR (126 MHz, DMSO-d_6) δ 172.54, 162.41, 157.97, 149.61, 145.15, 137.21, 135.96, 135.28, 131.58, 128.46, 128.31, 124.08, 119.97, 112.90, 99.54, 72.93, 71.50, 69.29, 69.19, 67.27, 63.46, 57.25, 53.19, 52.66, 35.87, 30.85, 22.60. HRMS (ESI+) calculated for $C_{132}H_{142}N_{20}O_{40}Zn$ $[M + 2H]^{2+}$: 1355.4248, found: 1355.4290; calculated for $C_{132}H_{143}N_{20}O_{40}Zn$ $[M + 3H]^{3+}$: 903.9682, found: 903.9683. HPLC analysis 2.38 min, 66.4% MeCN.

Glycocluster $\mathbf{3_d}$: Porphyrin $\mathbf{2_d}$ (30.0 mg) react with **SA** (43.6 mg) and CuBr.DMS (3.1 mg) to yield compound $\mathbf{3_d}$ as a purple solid after lyophilisation (48.3 mg, 74%). ^{1}H NMR (500 MHz, MeOD-d_4) δ 8.89–8.81 (m, 8H), 8.13 (m, 12H), 7.33 (s, 8H), 5.01 (d, J = 12.3, 4H), 4.76–4.68 (m, 12H), 4.45–4.36 (m, 8H), 4.10 (t, J = 5.1, 8H), 4.01 (dd, J = 5.9, 3.7, 8H), 3.91–3.86 (m, 4H), 3.79 (dd, J = 11.5, 2.5, 4H), 3.75–3.69 (m, 8H), 3.63–3.56 (m, 8H), 3.50 (dd, J = 9.2, 1.9, 4H), 2.88 (dd, J = 12.3, 3.7, 4H), 1.95 (s, 12H), 1.68 (t, J = 11.8, 4H). ^{13}C NMR (126 MHz, DMSO-d_6) δ 172.75, 157.99, 149.67, 144.74, 135.38, 131.79, 124.29, 120.02, 112.73, 100.29, 99.97, 99.58, 90.98, 76.22, 73.08, 72.93, 71.48, 69.19, 69.02, 67.09, 63.39, 57.39, 53.40, 53.24, 51.36, 49.49, 30.83, 22.60. HRMS (ESI+) calculated for $C_{116}H_{142}N_{20}O_{44}Zn$ $[M + 2H]^{2+}$: 1291.4385, found: 1291.4394; calculated for $C_{116}H_{143}N_{20}O_{44}Zn$ $[M + 3H]^{3+}$: 861.2947, found: 861.2956; calculated for $C_{116}H_{144}N_{20}O_{44}Zn$ $[M + 4H]^{4+}$: 646.2229, found: 646.2230. HPLC analysis 2.33 min, 64.9% MeCN.

Glycocluster $\mathbf{3_e}$: Porphyrin $\mathbf{2_e}$ (29.8 mg) react with **SA** (30.0 mg) and CuBr.DMS (2.1 mg) to yield compound $\mathbf{3_e}$ as a purple solid after lyophilisation (31.9 mg, 59%). ^{1}H NMR (500 MHz, MeOD-d_4) δ 8.85 (s, 8H), 8.10 (d, J = 8.3, 8H), 8.02 (s, 4H), 7.33 (d, J = 8.4, 8H), 4.96 (d, J = 12.1, 4H), 4.67 (d, J = 12.1, 4H), 4.53 (t, J = 5.1, 8H), 4.44–4.39 (m, 8H), 4.06–4.00 (m, 8H), 3.91–3.86 (m, 12H), 3.86–3.81 (m, 12H), 3.78–3.75 (m, 8), 3.74–3.68 (m, 16H), 3.67–3.60 (m, 24H), 3.51 (dd, J = 9.1, 1.7, 4H), 2.88 (dd, J = 12.0, 3.5, 4H), 2.00 (s, 12H), 1.61 (t, J = 11.6, 4H). ^{13}C NMR (126 MHz, DMSO-d_6) δ 172.50, 170.36, 158.06, 149.63, 144.33, 135.29, 131.66, 124.27, 120.02, 112.66, 99.85, 80.85, 76.25, 73.09, 71.53, 70.08, 69.96, 69.94, 69.89, 69.72, 69.66, 69.19, 69.07, 68.78, 67.40, 67.09, 63.37, 57.21, 53.07, 51.64, 49.38, 41.72, 22.61. HRMS (ESI+) calculated for $C_{140}H_{190}N_{20}O_{56}Zn$ $[M + 2H]^{2+}$: 1555.5958, found: 1555.5930; calculated for $C_{140}H_{191}N_{20}O_{56}Zn$ $[M + 3H]^{3+}$: 1037.3996, found: 1037.3984; calculated for $C_{140}H_{192}N_{20}O_{56}Zn$ $[M + 4H]^{4+}$: 778.3015, found: 778.3008; calculated for $C_{140}H_{193}N_{20}O_{56}Zn$ $[M + 5H]^{5+}$: 622.8427, found: 622.8431. HPLC analysis 2.33 min, 64.9% MeCN.

4.1.4. General procedure for glycoclusters $4_{a\text{-}e}$ synthesis

To as solution of porphyrins $\mathbf{2_{a\text{-}e}}$ (1 equiv.) and CuBr.DMS (0.6 equiv.) in DMSO (30 mg/mL) under argon was added 9-*O*-acetylated sialic acid **9-AcSA** (5 equiv.). The reaction mixture was stirred under microwave irradiation at 80 °C for 4 h. The product was precipitated by addition of DCM and the recovered solid was dissolved in water and treated with QuadrasilMP. The product was purified over size exclusion chromatography on Sephadex G-25 (elution: water).

Glycocluster $\mathbf{4_a}$: Porphyrin $\mathbf{2_a}$ (19.0 mg) react with **9-AcSA** (30.0 mg) and CuBr.DMS (2.2 mg) to yield compound $\mathbf{4_a}$ as a purple solid after lyophilisation (29.0 mg, 63%). Characterisations are in accordance with the literature [10].

Glycocluster $\mathbf{4_b}$: Porphyrin $\mathbf{2_a}$ (20.0 mg) react with **9-AcSA** (30.0 mg) and CuBr.DMS (1.9 mg) to yield compound $\mathbf{4_b}$ as a purple solid after lyophilisation (36.3 mg, 83%). ^{1}H NMR (500 MHz, MeOD-d_4) δ 8.82 (s, 8H), 8.00 (s, 12H), 7.19 (s, 8H), 5.01–4.92 (m, 4H), 4.68 (d, J = 12.0, 4H), 4.39 (d, J = 9.8, 12H), 4.17–4.03 (m, 16H), 3.78–3.71 (m, 8H), 3.68–3.63 (m, 4H), 3.50 (d, J = 9.7, 4H), 2.83 (d, J = 10.3, 4H), 2.03 (s, 12H), 2.00 (s, 12H), 1.97–1.91 (m, 8H), 1.90–1.84 (m, 8H), 1.72–1.64 (m, 4H), 1.62–1.52 (m, 8H), 1.52–1.44 (m, 8H), 1.42–1.34 (m, 8H). ^{13}C NMR (126 MHz, DMSO-d_6) δ 172.57, 170.63, 158.25, 149.63, 144.44, 135.28, 134.91, 131.64, 123.89, 120.04, 112.58, 72.70, 69.38, 68.78, 67.66, 67.15, 66.65, 57.38, 52.96, 49.38, 29.80, 28.92, 28.34, 25.99, 25.61, 22.59, 20.88. HRMS (ESI+) calculated for $C_{136}H_{174}N_{20}O_{44}Zn$ $[M + 2H]^{2+}$: 1427.5637, found: 1427.5655; calculated for $C_{136}H_{175}N_{20}O_{44}Zn$ $[M + 3H]^{3+}$: 952.0449, found: 952.0451; calculated for $C_{136}H_{176}N_{20}O_{44}Zn$ $[M + 4H]^{4+}$: 714.2855, found: 714.2840. HPLC analysis 2.78 min, 78.4% MeCN.

Glycocluster $\mathbf{4_c}$: Porphyrin $\mathbf{2_c}$ (13.6 mg) react with **9-AcSA** (20.0 mg) and CuBr.DMS (1.0 mg) to yield compound $\mathbf{4_c}$ as a purple solid after

lyophilisation (22.1 mg, 75%). ^{1}H NMR (500 MHz, MeOD-d$_4$) δ 8.85 (s, 8H), 8.08 (m, 12H), 7.67 (d, J = 7.8, 8H), 7.47 (d, J = 7.8, 8H), 7.38 (d, J = 8.2, 8H), 5.67 (s, 8H), 5.38 (s, 8H), 4.99–4.92 (m, 4H), 4.70 (d, J = 11.6, 4H), 4.35 (dd, J = 11.2, 1.5, 4H), 4.14–4.02 (m, 8H), 3.74–3.69 (m, 8H), 3.66–3.61 (m, 4H), 3.49 (d, J = 9.2, 4H), 2.86 (d, J = 10.9, 4H), 2.04 (s, 12H), 2.00 (s, 12H), 1.66–1.59 (m, 4H). ^{13}C NMR (126 MHz, DMSO-d_6) δ 177.07, 172.56, 170.62, 157.92, 149.54, 131.17, 135.79, 135.27, 131.61, 128.38, 128.27, 119.90, 112.86, 99.47, 92.61, 72.44, 69.21, 68.73, 66.62, 52.89, 22.48, 20.86. HRMS (ESI+) calculated for $C_{140}H_{150}N_{20}O_{44}Zn$ $[M + 2H]^{2+}$: 1439.4698, found: 1439.4724; calculated for $C_{140}H_{151}N_{20}O_{44}Zn$ $[M + 3H]^{3+}$: 959.9823, found: 959.9832; calculated for $C_{140}H_{152}N_{20}O_{44}Zn$ $[M + 4H]^{4+}$: 720.2385, found: 720.2412. HPLC analysis 2.48 min, 69.4% MeCN.

Glycocluster **4$_d$**: Porphyrin **2$_d$** (30.0 mg) react with **9-AcSA** (49.0 mg) and CuBr.DMS (3.1 mg) to yield compound **4$_d$** as a purple solid after lyophilisation (50.8 mg, 71%). ^{1}H NMR (500 MHz, MeOD-d$_4$) δ 8.86 (s, 8H), 8.18–8.08 (m, 12H), 7.33 (d, J = 7.8, 8H), 5.02–4.97 (m, 4H), 4.76–4.68 (m, 12H), 4.43–4.32 (m, 12H), 4.14–4.06 (m, 16H), 4.03–3.99 (m, 8H), 3.75–3.68 (m, 8H), 3.65–3.60 (m, 4H), 3.49–3.45 (m, 4H), 2.91 (d, J = 10.8, 4H), 1.99 (s, 12H), 1.96 (s, 12H), 1.71–1.64 (m, 4H). ^{13}C NMR (126 MHz, DMSO-d_6) δ 172.65, 170.63, 157.95, 149.62, 135.34, 131.64, 131.64, 124.33, 120.00, 112.66, 72.65, 69.41, 68.97, 68.80, 67.19, 66.68, 57.43, 53.04, 49.44, 22.52, 20.86. HRMS (ESI+) calculated for $C_{124}H_{150}N_{20}O_{48}Zn$ $[M + 2H]^{2+}$: 1375.4596, found: 1375.4590; calculated for $C_{124}H_{151}N_{20}O_{48}Zn$ $[M + 3H]^{3+}$: 917.3088, found: 917.3086; calculated for $C_{124}H_{152}N_{20}O_{48}Zn$ $[M + 4H]^{4+}$: 688.2334, found: 688.2338. HPLC analysis 2.38 min, 66.4% MeCN.

Glycocluster **4$_e$**: Porphyrin **2$_e$** (13.3 mg) react with **9-AcSA** (15.0 mg) and CuBr.DMS (1.0 mg) to yield compound **4$_e$** as a purple solid after lyophilisation (16.4 mg, 65%). ^{1}H NMR (500 MHz, MeOD-d$_4$) δ 8.84 (s, 8H), 8.08 (d, J = 7.9, 8H), 8.01 (s, 4H), 7.30 (d, J = 7.6, 8H), 5.01–4.93 (m, 4H), 4.65 (d, J = 11.5, 4H), 4.54–4.49 (m, 8H), 4.37 (d, J = 9.7, 10H), 4.14–4.06 (m, 10H), 4.02–3.96 (m, 8H), 3.88–3.83 (m, 8H), 3.83–3.79 (m, 10H), 3.77–3.67 (m, 30H), 3.66–3.60 (m, 32H), 3.48 (d, J = 8.7, 4H), 2.85 (d, J = 10.9, 4H), 2.02 (s, 12H), 2.00 (s, 12H), 1.67–1.60 (m, 4H). ^{13}C NMR (126 MHz, DMSO-d_6) δ 172.67, 170.66, 158.07, 149.65, 144.40, 135.31, 131.67, 124.25, 120.04, 112.65, 100.14, 72.66, 70.09, 69.94, 68.89, 69.72, 69.66, 69.42, 61.19, 68.80, 67.40, 67.22, 66.67, 57.30, 53.05, 49.39, 41.80, 22.58, 20.88. HRMS (ESI+) calculated for $C_{148}H_{198}N_{20}O_{60}Zn$ $[M + 2H]^{2+}$: 1639.6169, found: 1639.6201; calculated for $C_{148}H_{199}N_{20}O_{60}Zn$ $[M + 3H]^{3+}$: 1093.4137, found: 1093.4146; calculated for $C_{148}H_{200}N_{20}O_{60}Zn$ $[M + 4H]^{4+}$: 820.3121, found: 820.3124; calculated for $C_{148}H_{201}N_{20}O_{60}Zn$ $[M + 5H]^{5+}$: 656.4511, found: 656.4522. HPLC analysis 2.37 min, 66.1% MeCN.

4.2. Biology

4.2.1. Pseudoviral-based neutralization assay

The anti-infective activity of the glycosylated porphyrins was assessed using a pseudovirus-based neutralization test (pVNT). Replication-deficient Moloney murine leukemia virus (MuLV) particles pseudotyped with the SARS-CoV-2 spike protein (wild-type D614G, Alpha B.1.1.7, Delta B.1.617.2, JN.1, and KP.3) and encoding a firefly luciferase reporter gene were used as viral surrogates. Vero-E6 served as target cells for infection. Glycoclusters and control compounds were serially diluted (starting concentration 20 mM) and incubated with pseudoviruses for 2 h prior to cell exposure. Viral entry was quantified by measuring luciferase activity 48 h post-infection, which is proportional to the number of infected cells. Infectivity was normalized using standard controls pseudovirus-infected cells without compounds defined 100% infectivity, while uninfected cells (cells only) defined the 0% baseline. Results are expressed as the concentration required to inhibit 50% of the viral infection (IC_{50}). In the plots (SI) presenting the relative inhibition (%) as a function of dilution titer, the concentrations of molecules can be obtained by dividing the initial stock solution (20 mM) by the titer. The protocol was detailed in a previous publication [36].

4.2.2. Focispot assay

4.2.2.1. Cell line and cell culture. Vero-ACE2 cells were cultured in DMEM, supplemented with 2 mM glutamine, 100 U/mL penicillin, 100 mg/mL streptomycin and 10% FCS in 5% CO_2 37 °C incubator. Cells were free of mycoplasma contamination.

4.2.2.2. Virus culture. The SARS-CoV-2 Delta variants was produced on Vero-ACE2 cells. Cells were infected using MOI of 0.1 in high-glucose DMEM supplemented with 2% FCS, non-essential amino acids, 100 U/mL penicillin, and 100 mg/mL streptomycin. Following a 48-h incubation at 37 °C with 5% CO_2, the culture medium was harvested for virus purification. The supernatant was first clarified by centrifugation at 1200 rpm for 5 min at 4 °C to remove cell debris. The clarified supernatant was then subjected to a second centrifugation at 4800 rpm for 15 min at 4 °C. The resulting supernatant, containing the virus, was aliquoted and stored at −80 °C until further use. Viral titers were determined by $TCID_{50}$ assay on Vero-ACE2 cells using 10-fold serial dilutions of the viral stock. The $TCID_{50}$ was defined as the dilution at which 50% of wells displayed virus-induced cytopathic effect.

4.2.2.3. Focispot experiment procedure. Vero ACE2 cells were maintained in standard growth medium and incubated at 37 °C with 5% CO_2. For assays, cells were seeded in flat-bottom 96-well tissue-culture plates at a density of 1×10^4 cells per well and allowed to adhere overnight. The antiviral compound was prepared as a 10-fold serial dilution series ranging from 100 µM to 0.01 µM. For infection, 200 $TCID_{50}$ of virus were mixed with each compound dilution. Virus-compound mixtures were pre-incubated for 20 min at room temperature. Pre-incubated virus-compound mixtures were added to the cell monolayers. Plates were incubated for 2 h at 37 °C with 5% CO_2 to allow adsorption. Following adsorption, 100 µL per well of 2× carboxymethylcellulose (CMC) medium viscosity were added directly to each well to restrict viral spread. Plates were incubated for 1 day at 37 °C with 5% CO_2. After incubation, plate medium was removed and cells were fixed by adding 200 µL per well of 4% formaldehyde in PBS for 15 min at room temperature. Plates were washed four times with PBS (200 µL per well per wash). Cells were then permeabilized by adding 100 µL per well of ice-cold methanol (99.8%). To comply with BSL-3 exit procedures, a nocolysis decontamination cycle was applied for 2 h. Plates were washed again as above. Non-specific binding was blocked with 200 µL per well of PBS containing 1% BSA for 1 h at room temperature, followed by washes as above. For detection, 100 µL per well of MTCC25-biotinylated monoclonal antibody diluted to 1 µg/mL in PBS with 0.1% BSA were added and incubated for 1 h at room temperature. Plates were washed and then incubated with 100 µL per well of streptavidin–HRP diluted 1:1000 in PBS with 0.1% BSA for 1 h at room temperature. Plates were washed again as above. MB substrate for HRP was filtered through a 0.45 µm filter and 100 µL per well were added. Color was developed until distinct foci were visible (typically 5–30 min). Development was stopped by thorough washing in tap water. Plates were left to dry completely and stored protected from light at room temperature. Infectious foci were enumerated using the Mabtech IRIS2™ reader, and inhibition was quantified relative to virus-only controls to derive antiviral activity.

4.2.3. Cytotoxicity evaluation

The cytotoxicity of the molecules was evaluated using a crystal violet staining test. Vero-E6 cells were deposited in wells and the molecules to be tested were diluted in a series from 1/10 to 1/1000 and deposited on the cells. Twenty-four hours later, the supernatant was discarded, and the cells were fixed with 4% paraformaldehyde for 30 min. The living cells were then stained with a 1% crystal violet solution for 30 min. This

stain was then resuspended with methanol and the absorbance of the different wells was read at 580 nm using the SpectraMax iD3. A 2% Triton X solution was used as a positive control.

CRediT authorship contribution statement

Vivian Lioret: Writing – original draft, Methodology, Investigation, Data curation. **Constant Gillot:** Writing – review & editing, Formal analysis, Data curation. **Marie Hologne:** Writing – review & editing, Formal analysis, Data curation. **Jenny Ha:** Formal analysis, Data curation. **Dmytro Strilets:** Validation, Formal analysis, Data curation. **Laurent Lubrano Di Scampamorte:** Formal analysis, Data curation. **Laurent Gillet:** Writing – review & editing, Supervision, Formal analysis, Data curation. **Jonathan Douxfils:** Writing – review & editing, Supervision, Formal analysis, Data curation. **Stéphane P. Vincent:** Writing – review & editing, Validation, Supervision, Resources, Project administration, Funding acquisition, Conceptualization.

Declaration of Competing Interest

The authors declare the following financial interests/personal relationships which may be considered as potential competing interests: Stephane VINCENT has patent Acetylated sialic acid glycoclusters and their uses for treating infectious diseases pending to: Non-applicable. Stephane VINCENT has patent Porphyrine cycloclusters with antiviral activity pending to: Non-applicable. If there are other authors, they declare that they have no known competing financial interests or personal relationships that could have appeared to influence the work reported in this paper.

Acknowledgments

The authors are grateful to Fonds National de la Recherche Scientifique (FNRS, post-doctoral grant to VL (PDR T.0241.23), chargé de recherche position to DS) and Actions de Recherche Concertée (ARC, PhD grant to JH). The authors acknowledge the use of the UNamur technological platforms MaSUN, PC2, LOS and electron microscopy.

Appendix A. Supplementary data

Supplementary data to this article can be found online at https://doi.org/10.1016/j.bioorg.2026.109519.

Data availability

Data will be made available on request.

References

[1] N. Zhu, D. Zhang, W. Wang, X. Li, B. Yang, J. Song, X. Zhao, B. Huang, W. Shi, R. Lu, P. Niu, F. Zhan, X. Ma, D. Wang, W. Xu, G. Wu, G.F. Gao, W. Tan, N. Engl, J. Med. 382 (2020) 727–733.
[2] F. Krammer, Nature 586 (2020) 516–527.
[3] M. Hoffmann, H. Kleine-Weber, S. Schroeder, N. Krüger, T. Herrler, S. Erichsen, T. S. Schiergens, G. Herrler, N.H. Wu, A. Nitsche, M.A. Müller, C. Drosten, S. Pöhlmann, Cell 181 (2020) 271–280.
[4] L. Cantuti-Castelvetri, R. Ojha, L.D. Pedro, M. Djannatian, J. Franz, S. Kuivanen, F. van der Meer, K. Kallio, T. Kaya, M. Anastasina, T. Smura, L. Levanov, L. Szirovicza, A. Tobi, H. Kallio-Kokko, P. Österlund, M. Joensuu, F.A. Meunier, S. J. Butcher, M.S. Winkler, B. Mollenhauer, A. Helenius, O. Gokce, T. Teesalu, J. Hepojoki, O. Vapalahti, C. Stadelmann, G. Balistreri, M. Simons, Science 370 (2020) 856–860.
[5] T.M. Clausen, D.R. Sandoval, C.B. Spliid, J. Pihl, H.R. Perrett, C.D. Painter, A. Narayanan, S.A. Majowicz, E.M. Kwong, R.N. McVicar, B.E. Thacker, C.A. Glass, Z. Yang, J.L. Torres, G.J. Golden, P.L. Bartels, R.N. Porell, A.F. Garretson, L. Laubach, J. Feldman, X. Yin, Y. Pu, B.M. Hauser, T.M. Caradonna, B.P. Kellman, C. Martino, P. Gordts, S.K. Chanda, A.G. Schmidt, K. Godula, S.L. Leibel, J. Jose, K. D. Corbett, A.B. Ward, A.F. Carlin, J.D. Esko, Cell 183 (2020) 1043–1057.
[6] A.N. Baker, S.-J. Richards, C.S. Guy, T.R. Congdon, M. Hasan, A.J. Zwetsloot, A. Gallo, J.R. Lewandowski, P.J. Stansfeld, A. Straube, M. Walker, S. Chessa, G. Pergolizzi, S. Dedola, R.A. Field, M.I. Gibson, ACS Cent. Sci. 6 (2020) 2046–2052.
[7] X.-L. Sun, Glycobiology 31 (2021) 1245–1253.
[8] L. Nguyen, K.A. McCord, D.T. Bui, K.M. Bouwman, E.N. Kitova, M. Elaish, D. Kumawat, G.C. Daskhan, I. Tomris, L. Han, P. Chopra, T.-J. Yang, S.D. Willows, A.L. Mason, L.K. Mahal, T.L. Lowary, L.J. West, S.-T.D. Hsu, T. Hobman, S. M. Tompkins, G.-J. Boons, R.P. de Vries, M.S. Macauley, J.S. Klassen, Nat. Chem. Biol. 18 (2022) 81–90.
[9] L. Unione, M.J. Moure, M.P. Lenza, I. Oyenarte, J. Ereño-Orbea, A. Ardá, J. Jiménez-Barbero, Angew. Chem. Int. Ed. 61 (2022) e202201432.
[10] S.J.L. Petitjean, W. Chen, M. Koehler, R. Jimmidi, J. Yang, D. Mohammed, B. Juniku, M.L. Stanifer, S. Boulant, S.P. Vincent, D. Alsteens, Nat. Commun. 13 (2022) 2564.
[11] T. Maass, G. Ssebyatika, M. Brückner, L. Breckwoldt, T. Krey, A. Mallagaray, T. Peters, M. Frank, R. Creutznacher, Chem. Eur. J. 28 (2022) e202202614.
[12] W. Saso, M. Yamasaki, S.-I. Nakakita, S. Fukushi, K. Tsuchimoto, N. Watanabe, N. Sriwilaijaroen, O. Kanie, M. Muramatsu, Y. Takahashi, T. Matano, M. Takeda, Y. Suzuki, K. Watashi, PLoS Pathog. 18 (2022) e1010590.
[13] C.J. Buchanan, B. Gaunt, P.J. Harrison, Y. Yang, J. Liu, A. Khan, A.M. Giltrap, A. Le Bas, P.N. Ward, K. Gupta, M. Dumoux, T.K. Tan, L. Schimaski, S. Daga, N. Picchiotti, M. Baldassarri, E. Benetti, C. Fallerini, F. Fava, A. Giliberti, P. I. Koukos, M.J. Davy, A. Lakshminarayanan, X. Xue, G. Papadakis, L.P. Deimel, V. Casablancas-Antràs, T.D.W. Claridge, A.M.J.J. Bonvin, Q.J. Sattentau, S. Furini, M. Gori, J. Huo, R.J. Owens, C. Schaffitzel, I. Berger, A. Renieri, G.-C.M. Study, J. H. Naismith, A.J. Baldwin, B.G. Davis, Science 377 (2022) eabm3125.
[14] I. Tomris, L. Unione, L. Nguyen, P. Zaree, K.M. Bouwman, L. Liu, Z. Li, J.A. Fok, M. Ríos Carrasco, R. van der Woude, A.L.M. Kimpel, M.W. Linthorst, S. E. Kilavuzoglu, E.C.J.M. Verpalen, T.G. Caniels, R.W. Sanders, B.A. Heesters, R. J. Pieters, J. Jiménez-Barbero, J.S. Klassen, G.-J. Boons, R.P. de Vries, ACS Chem. Biol. 18 (2023) 1180–1191.
[15] X. Zhang, P. Hao, J. Mo, P.-Y. Wang, G. Wang, L. Li, X.-J. Zheng, X. Yuan, W. Yao, N. Jin, C. Li, X.-S. Ye, ACS Nano 18 (2024) 32910–32923.
[16] M. Dey, A. Sharma, G. Dhanawat, D. Gupta, K.H. Harshan, N. Parveen, ACS Infect. Dis. 10 (2024) 907–916.
[17] K.C. Siwak, E.V. LeBlanc, H.M. Scott, Y. Kim, I. Pellizzari-Delano, A.M. Ball, N. J. Temperton, C.J. Capicciotti, C.C. Colpitts, PLoS Pathog. 20 (2024) e1012365.
[18] M. Monti, E. Milanetti, M.T. Frans, M. Miotto, L. Di Rienzo, M.V. Baranov, G. Gosti, A.K. Somavarapu, M. Nagaraj, T.W. Golbek, E. Rossing, S.J. Moons, T.J. Boltje, G. van den Bogaart, T. Weidner, D.E. Otzen, G.G. Tartaglia, G. Ruocco, S.J. Roeters, J. Phys. Chem. B 128 (2024) 451–464.
[19] M. McCallum, J. Bassi, A. De Marco, A. Chen, A.C. Walls, J. Di Iulio, M.A. Tortorici, M.J. Navarro, C. Silacci-Fregni, C. Saliba, K.R. Sprouse, M. Agostini, D. Pinto, K. Culap, S. Bianchi, S. Jaconi, E. Cameroni, J.E. Bowen, S.W. Tilles, M.S. Pizzuto, S.B. Guastalla, G. Bona, A.F. Pellanda, C. Garzoni, W.C. Van Voorhis, L.E. Rosen, G. Snell, A. Telenti, H.W. Virgin, L. Piccoli, D. Corti, D. Veesler, Science 373 (2021) 648–654.
[20] J. Favresse, C. Gillot, J. Cabo, C. David, J.-M. Dogné, J. Douxfils, Int. J. Infect. Dis. 143 (2024) 107028.
[21] F. Kabinger, C. Stiller, J. Schmitzová, C. Dienemann, G. Kokic, H.S. Hillen, C. Höbartner, P. Cramer, Nat. Struct. Mol. Biol. 28 (2021) 740–746.
[22] M. Laporte, D. Jochmans, D. Bardiot, L. Desmarets, O.J. Debski-Antoniak, G. Mizzon, R. Abdelnabi, P. Leyssen, W. Chiu, Z. Zhang, N. Nomura, S. Boland, U. Ohto, Y. Stahl, J. Wuyts, S. De Jonghe, A. Stevaert, M.J. van Hemert, B. W. Bontes, P. Wanningen, G.J.M. Groenewold, A. Zegar, K. Owczarek, S. Joshi, M. Koukni, P. Arzel, H. Klaassen, J.-C. Vanherck, I. Vandecaetsbeek, N. Cremers, K. Donckers, T. Francken, T. Van Buyten, J. Rymenants, J. Schepers, K. Pyrc, R. Hilgenfeld, J. Dubuisson, B.-J. Bosch, F. Van Kuppeveld, C. Eydoux, E. Decroly, B. Canard, L. Naesens, B. Weynand, E.J. Snijder, S. Belouzard, T. Shimizu, R. Bartenschlager, D.L. Hurdiss, A. Marchand, P. Chaltin, J. Neyts, Nature 640 (2025) 514–523.
[23] E. Van Damme, P. Abeywickrema, Y. Yin, J. Xie, S. Jacobs, M.K. Mann, J. Doijen, R. Miller, M. Piassek, S. Marsili, M. Subramanian, L. Gottlieb, R. Abdelnabi, M. Van Gool, N. Van Den Broeck, I. De Pauw, A. Diels, P. Vermeulen, K. Temmerman, T. Scobey, M. Mattocks, A. Schäfer, D. Jochmans, S. De Jonghe, P. Leyssen, W. Chiu, M. Diosa Toro, M. Zwaagstra, A.A. Leijs, H.L.M. De Gruyter, C. Buyck, K. Van Den Heede, F. Jacobs, C. Van den Eynde, L. Thijs, V. Raeymaekers, S. Miller, A. Del Rosario, J. Neyts, D. Peeters, R.S. Baric, F.J.M. Van Kuppeveld, E.J. Snijder, M.J. Van Hemert, M. Monshouwer, S. Sharma, R. Draghia-Akli, A. Koul, M. Van Loock, Nature 640 (2025) 506–513.
[24] S. Cecioni, A. Imberty, S. Vidal, Chem. Rev. 115 (2015) 525–561.
[25] A. Muñoz, D. Sigwalt, B.M. Illescas, J. Luczkowiak, L. Rodríguez-Pérez, I. Nierengarten, M. Holler, J.S. Remy, K. Buffet, S.P. Vincent, J. Rojo, R. Delgado, J. F. Nierengarten, N. Martín, Nat. Chem. 8 (2016) 50–57.
[26] K.G. Leslie, S.S. Berry, G.J. Miller, C.S. Mahon, J. Am. Chem. Soc. 146 (2024) 27215–27232.
[27] N.J. Overeem, E. van der Vries, J. Huskens, Small 17 (2021) e2007214.
[28] J. Ramos-Soriano, J. Rojo, Chem. Commun. 57 (2021) 5111–5126.
[29] L. Su, Y. Feng, K. Wei, X. Xu, R. Liu, G. Chen, Chem. Rev. 121 (2021) 10950–11029.
[30] U.I.M. Gerling-Driessen, M. Hoffmann, S. Schmidt, N.L. Snyder, L. Hartmann, Chem. Soc. Rev. 52 (2023) 2617–2642.
[31] J. Patino-Alonso, J. Cabrera-González, J. Merino, G. Nieto-Ortiz, F. Lasala, J. Katati, C.H.B. da Cruz, A.K. Monnappa, P. Mateos-Gil, Á. Canales, I. López-Montero, B.M. Illescas, R. Delgado, N. Martín, Small 20 (2024) 2307045.

[32] J. Cramer, A. Lakkaichi, B. Aliu, R.P. Jakob, S. Klein, I. Cattaneo, X. Jiang, S. Rabbani, O. Schwardt, G. Zimmer, M. Ciancaglini, T. Abreu Mota, T. Maier, B. Ernst, J. Am. Chem. Soc. 143 (2021) 17465–17478.
[33] V. Porkolab, M. Lepšík, S. Ordanini, A. St John, A. Le Roy, M. Thépaut, E. Paci, C. Ebel, A. Bernardi, F. Fieschi, ACS Cent. Sci. 9 (2023) 709–718.
[34] S. Cecioni, J.-P. Praly, S.E. Matthews, M. Wimmerová, A. Imberty, S. Vidal, Chem. Eur. J. 18 (2012) 6250–6263.
[35] A. Bernardi, J. Jiménez-Barbero, A. Casnati, C. De Castro, T. Darbre, F. Fieschi, J. Finne, H. Funken, K.E. Jaeger, M. Lahmann, T.K. Lindhorst, M. Marradi, P. Messner, A. Molinaro, P.V. Murphy, C. Nativi, S. Oscarson, S. Penadés, F. Peri, R. J. Pieters, O. Renaudet, J.L. Reymond, B. Richichi, J. Rojo, F. Sansone, C. Schäffer, W.B. Turnbull, T. Velasco-Torrijos, S. Vidal, S. Vincent, T. Wennekes, H. Zuilhof, A. Imberty, Chem. Soc. Rev. 42 (2013) 4709–4727.
[36] C. Gillot, J. Favresse, V. Maloteau, J.M. Dogné, J. Douxfils, Bio-Protoc. 12 (2022) e4377.
[37] H. Ogura, K. Furuhata, S. Sato, K. Anazawa, M. Itoh, Y. Shitori, Carbohydr. Res. 167 (1987) 77–86.
[38] G.C. Daskhan, C. Pifferi, O. Renaudet, ChemistryOpen 5 (2016) 477–484.
[39] C. Gillot, C. David, J.-M. Dogné, J. Cabo, J. Douxfils, J. Favresse, Clin. Chem. Lab. Med. 63 (2025) e82–e85.
[40] C. Gillot, J.-L. Bayart, V. Maloteau, J.-M. Dogné, J. Douxfils, J. Favresse, Case rep. infect. dis. 2024 (2024) 9163490.
[41] M. Stefanelli, F. Mandoj, G. Magna, R. Lettieri, M. Venanzi, R. Paolesse, D. Monti, Molecules 25 (2020) 4544.
[42] X. Gong, T. Milic, C. Xu, J.D. Batteas, C.M. Drain, J. Am. Chem. Soc. 124 (2002) 14290–14291.
[43] A. Tikad, H. Fu, C.M. Sevrain, S. Laurent, J.-F. Nierengarten, S.P. Vincent, Chem. Eur. J. 22 (2016) 13147–13155.